AGU PUBLICATIONS

Tectonics

RESEARCH ARTICLE
10.1002/2013TC003381

Key Points:
- Structural domains of Malaspina Glacier
- Glacial morphology and flow reflect basal topography and structural geology
- Feature tracking of ice velocities on Malaspina Glacier

Supporting Information:
- Readme
- Figure S1
- Figure S2
- Figure S3

Correspondence to:
M. M. Cotton,
michellemariecotton@gmail.com

Citation:
Cotton, M. M., R. L. Bruhn, J. Sauber, E. Burgess, and R. R. Forster (2014), Ice surface morphology and flow on Malaspina Glacier, Alaska: Implications for regional tectonics in the Saint Elias orogen, *Tectonics*, *33*, doi:10.1002/2013TC003381.

Received 29 MAY 2013
Accepted 12 MAR 2014
Accepted article online 20 MAR 2014

Ice surface morphology and flow on Malaspina Glacier, Alaska: Implications for regional tectonics in the Saint Elias orogen

Michelle M. Cotton[1], Ronald L. Bruhn[1], Jeanne Sauber[2], Evan Burgess[3], and Richard R. Forster[3]

[1]Department of Geology and Geophysics, University of Utah, Salt Lake City, Utah, USA, [2]Planetary Geodynamics, NASA Goddard Space Flight Center, Greenbelt, Maryland, USA, [3]Department of Geography, University of Utah, Salt Lake City, USA

Abstract The Saint Elias Mountains in southern Alaska are located at a structural syntaxis where the coastal thrust and fold belt of the Fairweather plate boundary intersects thrust faults and folds generated by collision of the Yakutat Terrane. The axial trace of this syntaxis extends southeastward out of the Saint Elias Mountains and beneath Malaspina Glacier where it is hidden from view and cannot be mapped using conventional methods. Here we examine the surface morphology and flow patterns of Malaspina Glacier to infer characteristics of the bedrock topography and organization of the syntaxis. Faults and folds beneath the eastern part of the glacier trend northwest and reflect dextral transpression near the terminus of the Fairweather fault system. Those beneath the western part of the glacier trend northeast and accommodate folding and thrust faulting during collision and accretion of the Yakutat Terrane. Mapping the location and geometry of the structural syntaxis provides important constraints on spatial variations in seismicity, fault kinematics, and crustal shortening beneath Malaspina Glacier, as well as the position of the collisional deformation front within the Yakutat Terrane. We also speculate that the geometrical complexity of intersecting faults within the syntaxis formed a barrier to rupture propagation during two regional *Mw* 8.1 earthquakes in September 1899.

1. Introduction

In the Saint Elias Mountains, the Fairweather transform plate boundary forms a structural syntaxis with a thrust fault system actively accommodating accretion of the Yakutat Terrane to North America (Figure 1) [*Plafker,* 1987; *Estabrook et al.*, 1992; *Bruhn et al.*, 2004]. The geology of this structural bend or "syntaxis" lies partially underneath the Malaspina Glacier and has been subject to several studies that have mapped and analyzed the structural geology of the mountains that border Malaspina Glacier (Figure 1) [*Plafker,* 1987; *Bruhn et al.*, 2004; *Koons et al.*, 2010; *Chapman et al.*, 2012]; others have investigated the crustal seismicity and strain field associated with deformation beneath the glacier [*Savage and Lisowski*, 1986; *Estabrook et al.*, 1992; *Elliott*, 2011]. These studies confirmed the presence of active crustal deformation but provided little insight concerning the topography at the base of the glacier and how that topography relates to the structural geology. On the other hand, glaciological studies revealed variations in directions of ice flow, history of surging [*Muskett et al.,* 2008], and ice surface structure and thicknesses [*Allen and Sharp*, 1953; *Sharp*, 1958; *Sauber et al.*, 2005; *Conway et al.*, 2009; *Rignot et al.*, 2013]. Although these studies provided information on basal topography, they did not focus on the underlying geological structure.

The Saint Elias orogen of Yukon, Canada, and southern Alaska is unusual because of the extent to which glaciers cover the significant tectonic boundaries. The inability to directly observe and map these regional-scale structures severely inhibits development of a robust structural framework for the orogen. This motivated us to use glacier flow patterns and glacier surface morphology to infer the nature of the topography at the base of the ice, and hence constrain the locations and kinematics of buried structures [*Ford et al.*, 2003; *Bruhn et al.*, 2010, 2012]. The work reported herein on Malaspina Glacier completes our coverage of major, ice-covered structural boundaries within the Saint Elias orogen.

Our research goal was to investigate the structural geology beneath Malaspina Glacier and to determine how the structures relate to plate motion and active deformation. We found that the glacier is divided into two sectors with different patterns of ice flow and surface topography. The eastern sector flows toward the southeast over a substrate that parallels the structural trend of the coastal mountain's thrust belt southeast of

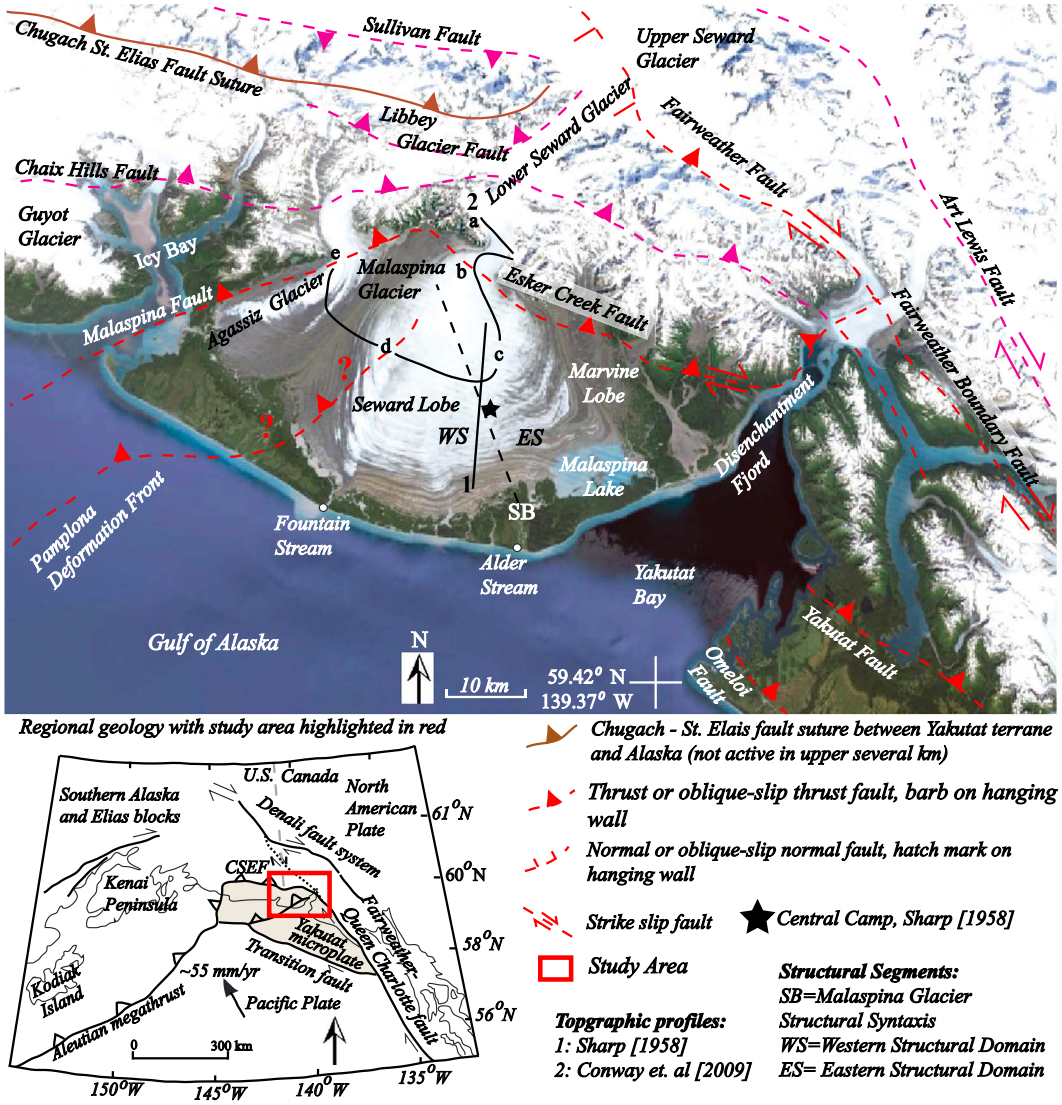

Figure 1. Tectonic map of Malaspina Glacier and surrounding areas showing the major faults. The axial trace of the structural syntaxis beneath Malaspina Glacier is labeled SB. The axis of the syntaxis separates the glacier into eastern and western structural domains (WS and ES). The eastern domain is underlain by northwest trending topography and structure whilst the western domain is underlain by northeast trending topography and structure. Currently active structures are shown in red; those that may be active are marked in purple. The Chugach-Saint Elias fault (brown) is the original tectonic suture between North America and the Yakutat Terrane. The area covered by the figure is marked by the red rectangle on the plate tectonic map in lower left-hand corner of the figure. This figure is modified from two figures originally published by *Bruhn et al.* [2012].

Yakutat Bay. This thrust belt absorbs ~0.4 mm/yr convergence out of ~50 mm/yr dextral motion because of transpression across the Fairweather transform plate boundary (Figure 1) [*Elliott*, 2011]. The western sector flows over basal topography and drainages that trend north to northeast, a structural trend that parallels the Malaspina Fault system and Pamplona Zone (Pamplona deformation front), which absorb ~1 cm/yr of crustal shortening within the deforming part of the Yakutat Terrane (Figure 1) [*Savage and Lisowski*, 1986; *Chapman et al.*, 2012; *Elliott*, 2011]. The zone of intersection between these two structural domains extends northwestward beneath Malaspina Glacier into the eastern Saint Elias Mountains.

Mapping the structural domains beneath Malaspina Glacier provides, for the first time, a geological framework for (1) the most intense locus of crustal seismicity within the collisional orogen, (2) constraining the position of faults and folds that must accommodate ~1 cm/yr shortening beneath the glacier [*Elliott*, 2011], and (3) reinterpreting how piedmont structures extend offshore into the Pamplona deformation front,

which marks the easternmost belt of active deformation within the accreting Yakutat Terrane. Lastly, we suggest that complex deformation within the core of the structural syntaxis creates an earthquake rupture barrier. A time delay of only 6 days between two *Mw* 8 earthquakes that ruptured large areas on either side of the glacier in September 1899 [*Tarr and Martin*, 1912; *Plafker and Thatcher*, 2008] supports the rupture barrier hypothesis. The data and observations that support these conclusions and speculations are presented following a brief presentation of the tectonic setting and research methods.

2. Tectonic and Glaciological Background

2.1. Tectonics and Geologic Setting of Malaspina Glacier

The name Malaspina Glacier actually refers to three glaciers Agassiz, Seward, and Marvine Glaciers that coalesce on the piedmont of the Saint Elias Mountains, creating a broad fan-shaped body of ice that is ~45 km long (north-south) and up to 75 km wide (Figure 1). Complexly folded lateral moraines separate the glaciers and attest to a history of glacial surging [*Muskett et al.,* 2008]. The Seward lobe of Malaspina Glacier is further divided into western and eastern sectors, which surge independent of one another (Figure 1).

The presence of two disparate structural domains beneath Malaspina Glacier is suggested by geological mapping in the adjacent mountains [*Plafker*, 1987; *Bruhn et al.*, 2004; *Chapman et al.*, 2012] and by seismologic and geodetic studies of the kinematics of faulting and crustal strain measurements [*Horner,* 1983; *Estabrook et al.*, 1992; *Savage and Lisowski,* 1986; *Elliott*, 2011]. The abrupt change in structural regime surrounding the glacier is created within the transition from dextral transpression along the Fairweather fault part of the transform plate boundary to collision and accretion of the Yakutat Terrane (Figure 1). Southeast of Malaspina Glacier the Yakutat microplate moves northwest relative to North America at ~50 mm/yr with ~0.4 mm/yr crustal shortening in the coastal mountains thrust belt (Figure. 1) [*Elliott*, 2011]. West of the glacier, the ratio of thrust to strike-slip fault motion increases dramatically where active faults strike northeastward. The upper crust of the microplate, which forms the accreted Yakutat Terrane, is stripped from the crystalline basement, imbricated, and shortened by folding and faulting on northeast striking thrust faults (Figure 1). This change in the intensity and style of deformation begins where the thickest crust, and hence most gravitationally buoyant part, of the Yakutat microplate impinges into the bend or "syntaxis" in the plate boundary at the northwestern end of the Fairweather fault [*Bruhn et al.*, 2004; *Chapman et al.*, 2012; *Worthington et al.*, 2012].

Geophysical observations provide the primary evidence for deformation beneath Malaspina Glacier. The presence of two disparate structural domains, one striking northwest and the other northeast, is evident from analysis of crustal seismicity [*Estabrook et al.*, 1992; *Doser*, 2012], geodetic data [*Savage and Lisowski*, 1986; *Elliott*, 2011], and by dislocation modeling of faulting during an *Mw* 8.1 earthquake on 10 September 1899 [*Plafker and Thatcher*, 2008]. Earthquake focal mechanisms indicate a complex stress field that activates thrusting on northeast striking faults beneath the northwestern part of the glacier [*Doser*, 2012]. The structural intersection between the Malaspina and Esker Creek faults defines one hinge line within the axial surface of the structural syntaxis created by the two disparate fault systems that bound and lie beneath Malaspina Glacier. Recently, *Elliott* [2011] proposed that a northeast striking thrust fault extends beneath the central part of the glacier based on modeling of GPS geodetic measurements that reveal ~1 cm/yr crustal shortening (Figure 1). Evidence for northwest striking faults beneath the eastern part of the glacier includes a north-northwest trending band of crustal earthquakes that define a fault near the confluence of Marvine and Malaspina Glaciers [*Estabrook et al.,* 1992] and dislocation modeling of coseismic rupturing on 10 September 1899 that requires thrusting on the Esker Creek fault beneath the head of the glacier (Figure 1) [*Plafker and Thatcher,* 2008].

2.2. Glaciology Background

Upper Seward Glacier is the primary source of ice for Malaspina Glacier (Figure 1). Ice flows out of the alpine basin of Upper Seward Glacier, down the range front through the narrow trough of Lower Seward Glacier, and discharges onto the piedmont where it crosses the Esker Creek fault at an ice surface elevation of ~600 m (Figure 1). Ice-penetrating radar measurements indicate that the Esker Creek fault is located in a several kilometer wide trough that is ~400 m deep at the range front (Figure 2a, locality b) [*Conway et al.,* 2009]. Farther downslope, the glacier occupies a broad bowl that is ~300 m below sea level beneath the central part of the glacier and rises toward sea level near the terminus (Figures 1 and 2b) [*Sharp*, 1958; *Molnia and Jones,*

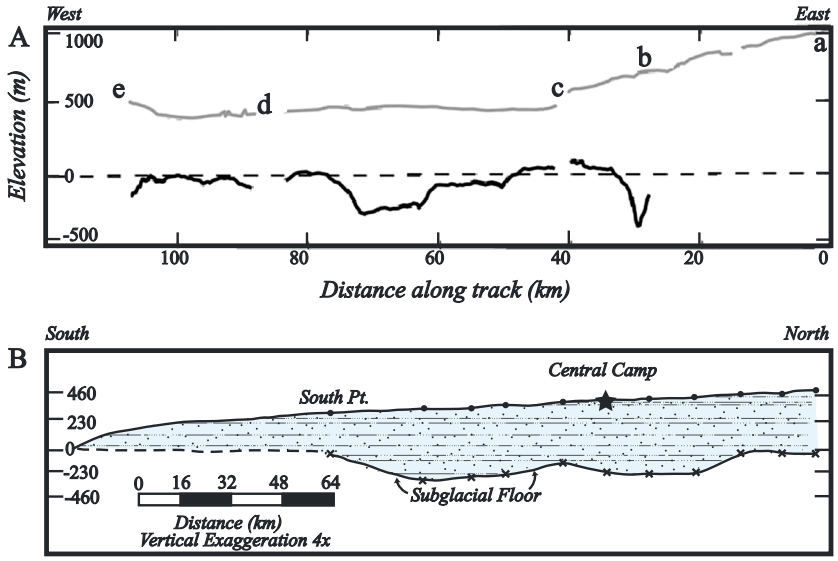

Figure 2. The basal topography of parts of Malaspina Glacier reported by *Conway et al.* [2009] and *Sharp* [1958]. (a) Ice thickness profile created from an airborne ice-penetrating radar survey (modified from *Conway et al.* [2009]). The profile is marked by track 2 on the glacier in Figure 1. The light gray line is the surface of the glacier and the black line marks the basal topography. (b) The base of the glacier mapped by seismic profiling and modified from an illustration in *Sharp* [1958]. See Figure 1, profile line 1 for location. Central camp on the surface of the glacier is also marked on Figure 1 by a star for reference.

1989; *Rignot et al.,* 2013]. The bowl is presumably eroded into Tertiary strata of the Yakutat Terrane, but there is most likely an intervening layer of till between the bedrock and overlying ice [*Sharp*, 1958].

Two transects across the glacier show the basal topography. *Allen and Sharp* [1953] and *Sharp* [1958] used seismic reflection and gravity to measure ice thickness and basement topography along a 16 km long line on the east central part of the glacier (Figure 1, topographic profile 1, 2B). They found two ridges separated by ~6 km with amplitudes that varied from >100 m for one ridge to several tens of meters for the other (Figure 2b). A 2-D gravity survey between Central Camp (Figures 1 and 2b) and the northern end of the profile revealed an elongated northwest trending ridge at the base of the glacier [*Allen and Sharp*, 1953].

The airborne ice-penetrating radar transect presented and discussed in *Conway et al.* [2009] began at the head of Malaspina Glacier, extended downslope, and then turned westward ending where Agassiz Glacier discharges onto the piedmont (Figure 1, topographic profile 2). The base of the glacier undulates with amplitudes of tens of meters (Figure 2a). Features that stand out include the deep trough of the Esker Creek fault at the head of the glacier and a large subglacial valley located between transect distances 60 km and 78 km with a floor that slopes gently westward between ~ −200 m to −250 m (Figure 2a). We will show that this valley lies beneath a tongue of flowing ice that extends southward more than 40 km from the head of Malaspina Glacier to its terminus at Fountain Stream, and which flows more rapidly than adjacent parts of the glacier.

The surface manifestation of the basal topography is highlighted by an extensive network of shallow troughs on the surface of the Seward lobe (Figure 3) [*Molnia and Jones,* 1989]. The intertwined and branching pattern of the troughs suggests that the surface of the glacier sags above an extensive system of meltwater drainage channels, some of which emerge as streams and rivers at the glacier's terminus [*Gustavson and Boothroyd*, 1987]. *Molnia and Jones* [1989] suggested that the troughs are surface manifestations of elongated "fjord-shaped" valleys at the base of the glacier. The network has persisted for at least several decades since it was first recognized, although individual troughs change appearance because of temporal variations in snow cover and ice flow. The trough network extends south from ~10 km below the head of the Seward lobe toward the ice terminus between Fountain and Alder Streams (Figure 3).

The piedmont lobe of Agassiz Glacier flows along the crest and steep southeastern dipping limb of a fault propagation fold that is cored by the Malaspina Fault (Figure 1) [*Chapman et al.,* 2012]. This location and the

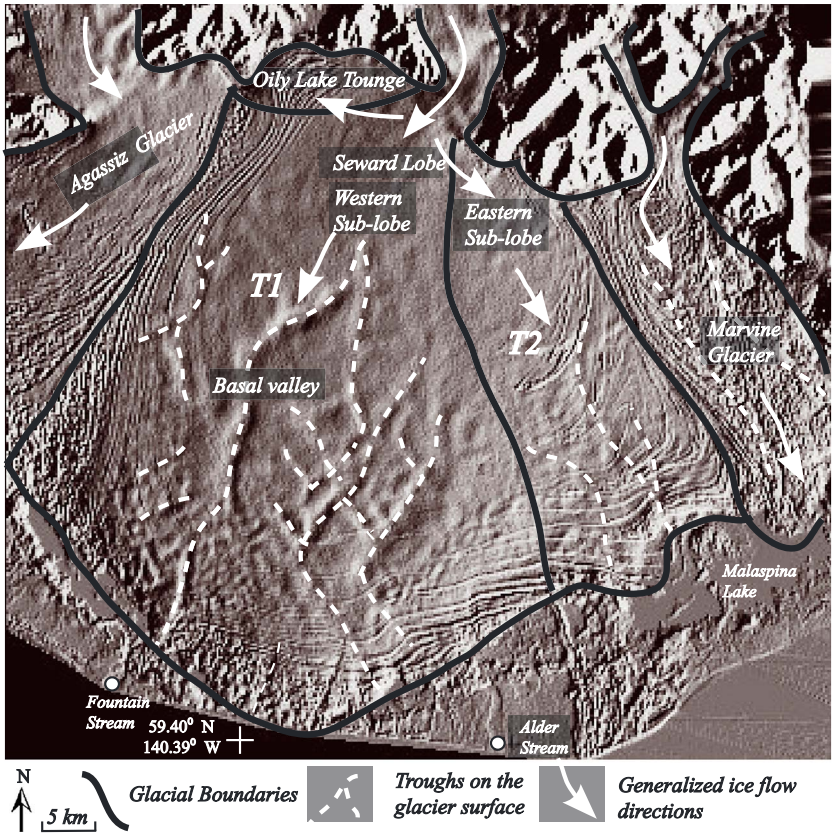

Figure 3. Shaded relief image of the surface of Malaspina Glacier acquired by SRTM in January 2000. Prominent troughs discussed in the text are highlighted in white and illustrate a complex pattern of surface troughs and ridges that partly reflect englacial and basal drainage conduits and topography. These surface features are also shown in an Airborne Terrane Mapper profile taken across the glacier (see Figure S2).

geometry of the fold are constrained by a balanced geological cross section that uses structural data from the mountain block on the western side of the glacier and data from an exploration drill hole that penetrated the fault several kilometers inland from Icy Bay near the glacier's terminus. The ice is ~450–500 m thick where crossed by the ice-penetrating radar transect, and then thickens near the end of the profile which crosses into the throat of the valley through which ice discharges onto the piedmont (Figure 2a). Just west of point d on the radar transect where Agassiz and Seward lobe merge beneath the wide moraine band, the elevation across Agassiz Glacier piedmont stays relatively constant.

The flow of Marvine Glacier is located above a linear band of northwest trending earthquakes that presumably define a crustal fault at depth [*Estabrook et al.,* 1992]. However, no data concerning ice thickness or basal topography in this area have been published as of the time of writing.

3. Research Methods

3.1. Ice Flow Over Basal Topography

Theoretical models relating the surface and subtle (relative to the ice thickness) basal properties of glaciers provide a useful guide for interpreting the influence of basal topography on the morphology and dynamics of Malaspina Glacier [*Gudmundsson*, 2003; *Raymond and Gudmundsson,* 2005]. Theoretical models indicate that basal perturbations in topography produce predictable changes in glacier surface morphology, velocity, and strain rate [*Gudmundsson*, 2003]. To supplement these studies, we conducted laboratory modeling experiments to aid interpretations of glacier surface properties created by ice flow over basal ridges at variable orientations (see Figure S1 in the supporting information).

3.2. Measurements of Glacier Topography and Velocity

Measurements of glacier flow velocity were done by tracking ice displacement using sequential acquisitions of optical imagery and synthetic aperture radar (SAR) scenes obtained at monthly to yearly time intervals. Surface features were also mapped using variations in ice surface reflection intensity on Landsat thematic mapper (TM) scenes and one side-looking airborne radar (SLAR) scene [*Molnia and Jones*, 1989]. The temporal persistence of features on the surface of the glacier was evaluated by comparing imagery obtained over several decades.

Data sets used for topographic analyses included digital elevation data from the Shuttle Radar Topographic Mapping mission (SRTM, Version 1) [*Farr and Kobrick*, 2000; *Muskett et al.*, 2003, 2008] and elevation profiles, contained in the supporting information, from NASA's Airborne Terrane Mapper (Figure S2) [*Krabill et al.*, 2002].

Ice flow velocity was measured by tracking the movement of surface features on time series of Landsat TM scenes and on a pair of ALOS Phased Array L-Band Synthetic Aperture Radar (PALSAR) scenes [*Rosenqvist et al.*, 2007]. Optical feature tracking using Landsat TM data measured surface velocities on the glacier at monthly (19 July 2007 to 11 August 2007) to annual periods (28 July 1999 and 2 August 2000) by image cross correlation [*Leprince et al.,* 2007a, 2007b]. Accuracy in image coregistration was determined by measuring displacements on both the glacier surface and stable ground (i.e., no ice or clouds); displacements on the stable ground indicated how well images were aligned to one another [*Turrin et al.*, 2013]. The mean of these displacements was subtracted from those of the original displacement field and resulted in a mean residual error of 1/16 of a pixel or ±5 m for 30 m Landsat TM/Enhanced Thematic Mapper Plus data.

Editing of the velocity vector field was done through visual inspection and was required to filter out inaccurate or erroneous velocities. SAR offset tracking was performed using GAMMA® software [*Strozzi et al.*, 2002] and the methods described in *Burgess et al.* [2013]. These velocity data have a root-mean-square error of 0.04 m d^{-1} and an overall directional bias of $<$0.005 m d^{-1}. Here we present data from a pair of ALOS PALSAR scenes acquired on 21 December 2007 and 5 February 2008.

Strain rates on the surface of the glacier were calculated from the surface velocities using SSPX software [*Cardozo and Allmendinger*, 2009] and show the orientations and rates of the principal stretches.

4. Observations and Results

4.1. Malaspina Glacier

Ice velocity maps of the Seward lobe of the Malaspina Glacier derived from ALOS PALSAR (Figure 4) and Landsat TM scenes (Figure 5) revealed that the glacier is divided into western and eastern sectors with the different directions of dominant ice flow denoted by ice tongues T1 and T2 on the map in Figures 4 and 5. Flow tongue T1 extends from the head of the glacier to the terminus at Fountain Stream. Ice tongue T2 extends southeastward from the head of the glacier to Malaspina Lake. In both ice tongues, the velocity decreases downslope where the ice spreads radially outward away from the flow tongue creating radial shortening and circumferential extensional flow on the lower part of the glacier [*Sharp,* 1958]. A third, subsidiary band of ice flows westward along the trough of the Esker Creek fault to Oily Lake where the Esker Creek and Malaspina Faults intersect beneath the Samovar Hills (Figures 3 and 4).

Three observations suggest that the T1 flow tongue is controlled by the morphology and hydrology of a large subglacial drainage network: (1) The wide basal valley detected by airborne ice-penetrating radar lies directly beneath the flow tongue (Figures 4 and 5), and (2) the elongated trough on the surface of the glacier that directly overlies the basal valley and extends roughly from Lower Seward Glacier down glacier toward the terminus (Figures 2 and 3). Subglacial drainage networks are 11 times more sensitive to surface topography than bed topography; thus, the observed surface trough is a strong indication of the location of a subglacial channel. The emergence of fountain stream at a coincident location confirms this observation [*Cuffey and Paterson*, 2010]. (3) Sedimentary detritus discharged from Fountain Stream contains grains of metamorphic rock derived from terrain beneath Upper Seward Glacier, more than 70 km away in the interior of the Saint Elias mountain range [*Enkelmann et al.,* 2009]. These lines of evidence support our contention that ice tongue T1 follows a large basal drainage system that occupies the deep valley detected on the ice-penetrating radar transect (Figures 4 and 5) [*Conway et al.,* 2009; *Molnia and Jones*, 1989].

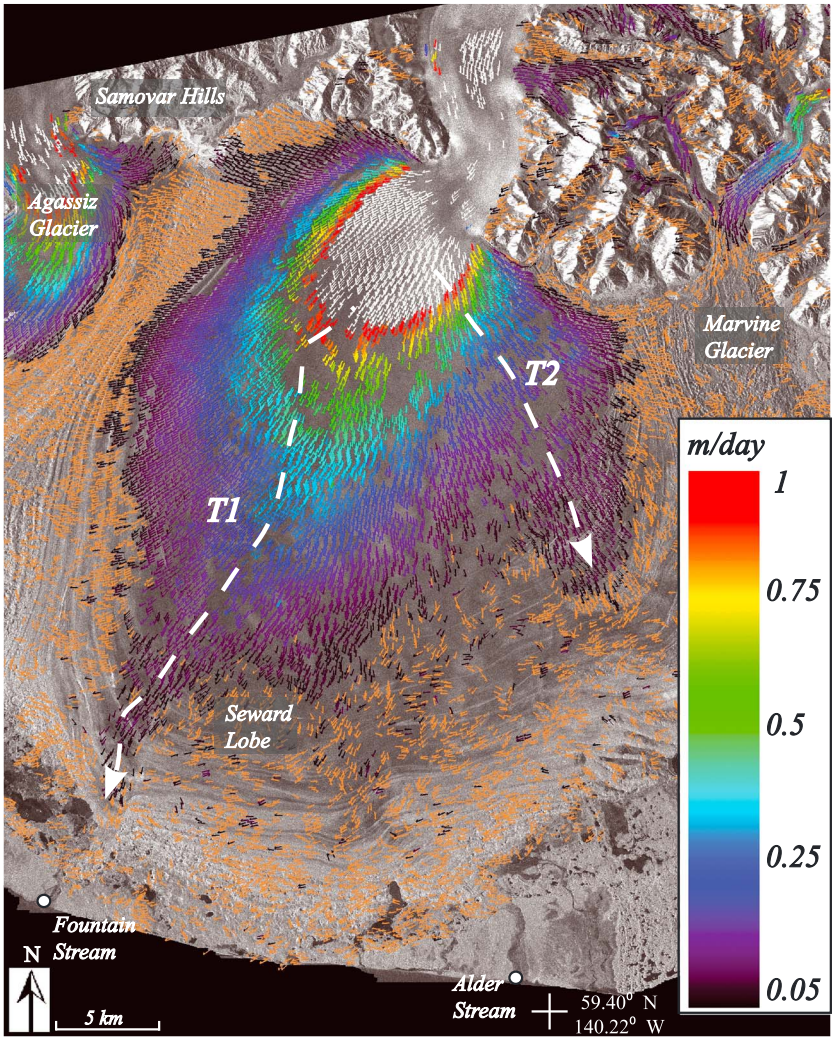

Figure 4. Ice flow velocity on the surface of Malaspina Glacier estimated by feature offset tracking of a pair of ALOS PALSAR scenes acquired on 21 December 2007 and 5 February 2008. T1 and T2 are major tongues of rapid flow.

The second large tongue of ice diverges from the head of the glacier and flows southeastward toward Malaspina Lake and the shore of Yakutat Bay. The presence of T2 is evident by close inspection of the ALOS PALSAR velocity map (Figure 4, arrow T2). However, the significance of T2 is most evident when inspecting a pair of Landsat TM scenes, acquired on 11 September 1986 and 29 August 1987, and obtained during a period of glacier surging (Figure 6). Large ice displacements during the surge refolded moraine loops on the glacier upslope from Malaspina Lake when the terminus advanced several kilometers toward the coast (Figures 6b and 6c) [*Muskett et al.*, 2008]. The tight hinges and subparallel limbs of the refolded moraine loops are a hallmark of ice flow around a buried bedrock ridge that is elongated in the direction of ice flow (Figures 6c and S1) [*Roush et al.*, 2003; *Bruhn et al.*, 2010]. This northwest-southeast elongated ridge is denoted "E2" in Figures 6 and 7. This is the second northwest trending ridge identified beneath the eastern part of the glacier. The first, marked E1 in Figure 7, was identified by gravity measurements in the early 1950s [*Allen and Sharp*, 1953].

Given the region of northwest topographic grain beneath the eastern part of the glacier, we searched for the boundary between that domain and the northeast trending structural domain beneath the western part of Malaspina Glacier. We began by inspection of the velocity maps (Figures 4 and 5) and then computed a strain rate map from the annual average velocity field on the lower part of the glacier. The rationale was that the spatial pattern of strain rate axes is sensitive to the presence of basal ridges that

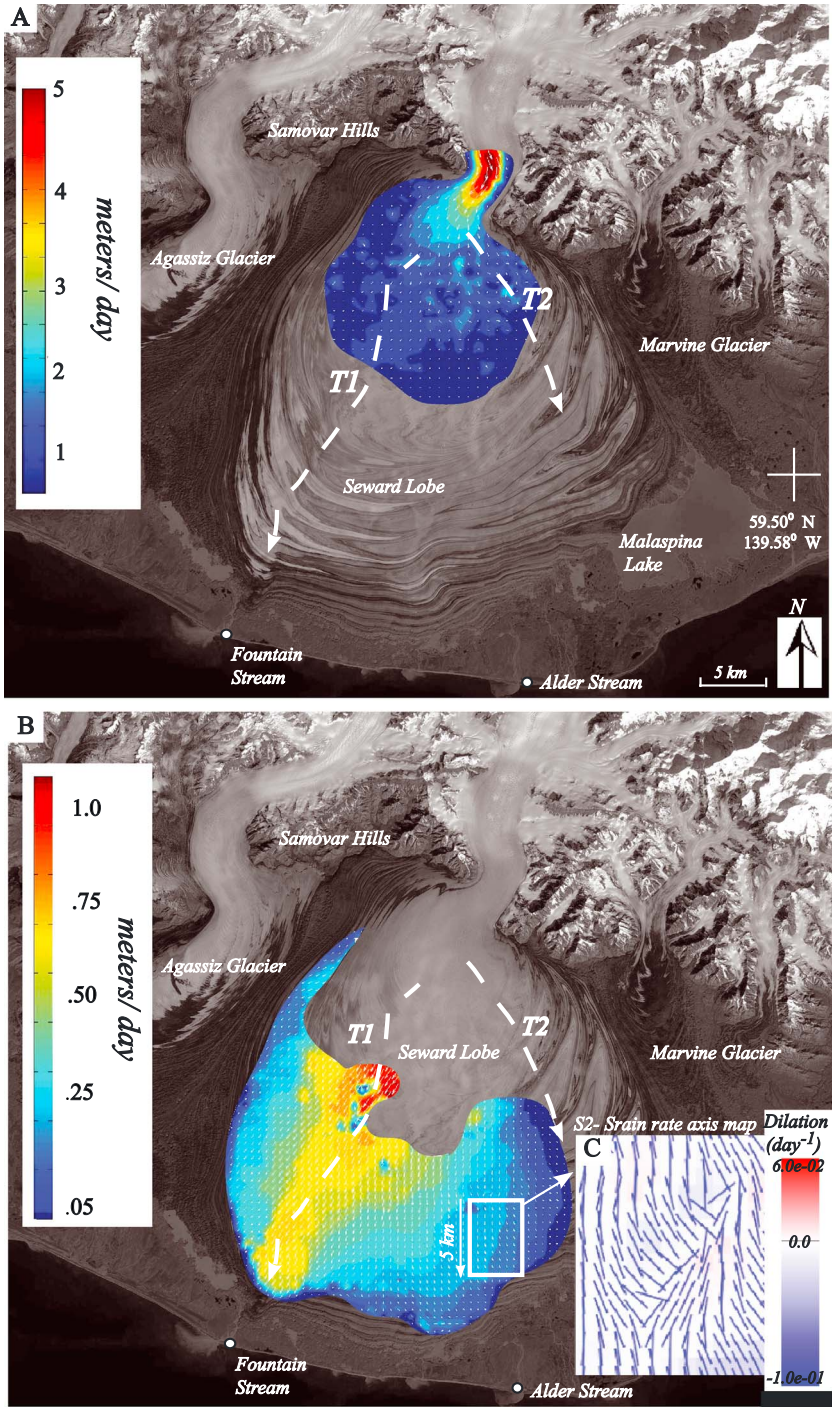

Figure 5. Ice flow velocity on the surface of the Seward lobe of Malaspina Glacier determined by optical feature tracking of Landsat scenes during two separate time intervals. The velocity field on the upper part of the lobe was calculated using two scenes acquired approximately 1 month apart (19 July to 11 August 2007) and is contoured in units of m/d. The white dashed line with arrowhead indicates prominent directions of ice flow above a large tunnel valley drainage system that extends from the head of the lobe to the terminus at Fountain Stream. Slower velocities in the lower part of the Seward lobe were determined from offsets of features between scenes obtained on 28 July 1999 and 2 August 2000, with contours in m/d. The small inset in the lower right is a strain rate axis map for the area encompassed by the black rectangle on the southeastern part of the Seward lobe. This strain rate axis pattern is similar to that expected where ice flows over a northeast elongated ridge.

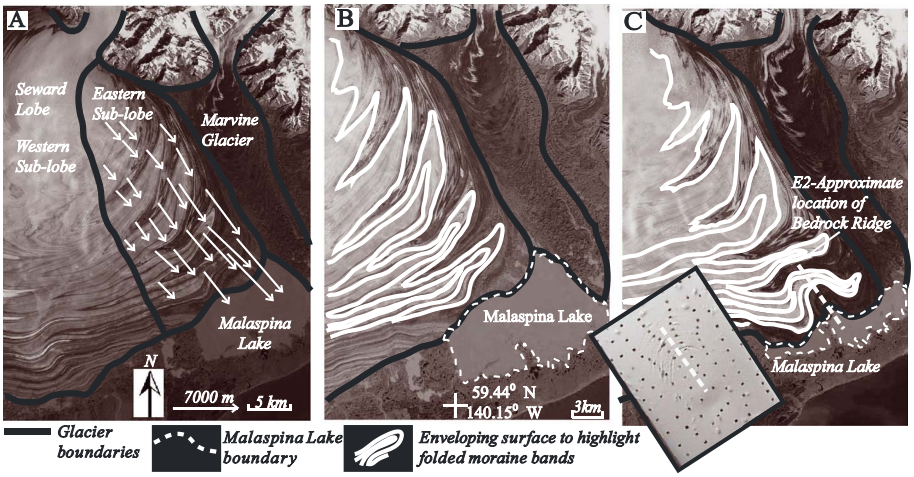

Figure 6. Displacements on the surface of the easternmost part of the Seward lobe during a glacier surge in 1986–1987. The very large displacements required tracking of features on the surface by hand. Note the refolding of the moraine loops in the center and right panels about a northwest trending axial surface in the lower part of the lobe above Malaspina Lake, indicating the presence of a bedrock ridge beneath the glacier. The small inset shows an experimentally derived surface feature of an elongated ridge created from an analog glacier model of a glacier (see Figure S1 in the supporting information for further discussion on the model).

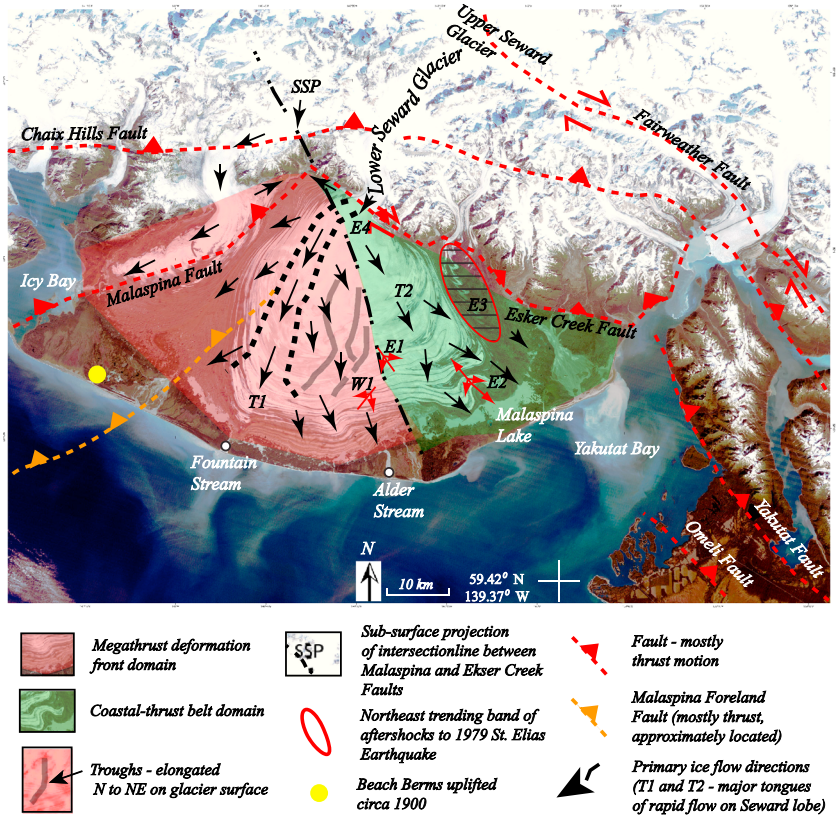

Figure 7. Structural domains beneath Malaspina Glacier created by the intersection between the northwest trending coastal ranges thrust belt and the northeast trending accretionary thrust faults.

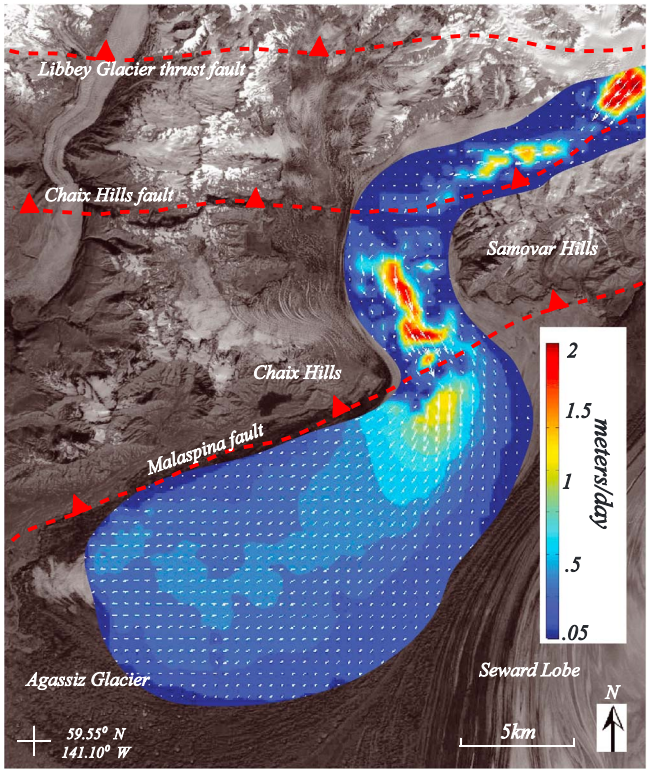

Figure 8. Annual averaged ice surface velocity map for surface of Agassiz Glacier between 21 December 2007 and 28 February 2008 computed by feature tracking of Landsat scenes. The highest velocities occur where the glacier flows over a topographic ramp of elevated slope located above the trace of the Libby thrust fault and down the ramp that leads southeastward from the alpine valley of the glacier onto the piedmont.

deflect ice flow at the surface, a topic we explored by experiments with several analog glacier models (see Figure S1).

There is an anomalous area several kilometers southwest of ridge E1 where the spatial pattern of strain rate axes suggests the presence of an ice-covered ridge that trends northeast, instead of northwest. The principal directions of shortening strain rate within that area were plotted as short line segments in the inset rectangle shown on the velocity map of the lower part of the glacier (Figure 5c). Proceeding from northwest to southeast in the direction of ice flow, the shortening axes first curve toward the southeast, then abruptly rotate northeast before curving back toward the south to southeast; this pattern mimics that predicted by both theory and experiment for a situation in which ice flows up and over a northeast elongated ridge located at depth. If this interpretation is correct, then the boundary between the two structural domains (northwest versus northeast structural trends) must lie between E1 and W1 in Figure 7. This conclusion is also supported by projecting the trace of the intersection line between the Esker Creek and Malaspina Faults onto the surface of Malaspina Glacier. The intersection trace projects southeastward from the base of the Samovar Hills toward the area between ice-buried features E1 and W1 (Figure 7).

4.2. Agassiz Glacier

The pattern of ice flow on the surface of Agassiz Glacier was estimated from an elevation of 1000 m on the flank of the Saint Elias range to the terminus on the outwash plain adjacent to Icy Bay (Figure 8). The upper limit of mapping was determined by the summer snow line, above which it was not possible to apply optical feature tracking. The rate of movement on the alpine section of the glacier between 21 December 2007 and 28 February 2008 varied from several meters per year up to 2 m per day (~700 m per year). The greatest velocities were located near the base of the ice ramp near the Libbey Glacier thrust fault (Figure 8) [*Chapman et al.*, 2012], within a narrow belt about 5 km long where the glacier flows along the subcrop of the Chaix Hills thrust fault and within the structurally controlled saddle between the Samovar and Chaix Hills that leads to the piedmont (Figure 8). The higher flow rates in these three areas are hypothesized to be a consequence of the structure of the substrate and the lithology.

The ice ramp at the Libbey Glacier thrust fault is likely created by differential erosion where indurated Cretaceous mélange is thrust atop well-bedded sandstone and shale of younger Cretaceous age (Figure 8) [*Chapman et al.*, 2012]. The bedding in the sandstone and shale unit is more susceptible to glacial abrasion and plucking than the overlying mélange, which forms a resistant caprock that steepens the glacier's slope. Glacial erosion is presumably focused along the fault because it was uplifted and tilted westward above the zone of intersection between the Malaspina and Esker Creek thrust faults (Figure 1). This structural geometry may explain why the band of higher flow rate is localized along the southeastern side of the valley, rather than in the center. Deformation around the Malaspina-Esker Creek fault intersection zone also decreases

toward the southwestern end of the Samovar Hills, which are warped upward at their northern end, creating the structural saddle that funnels ice moving 1 to 2 m per day (500 to 700 m per year) onto the piedmont. The topographic ramp between the alpine and piedmont sections of the glacier is located where the glacier flows across the gently dipping "back-limb" of Malaspina Fault propagation fold [*Chapman et al.*, 2012]. The higher ice velocities within the saddle do not reflect the position of the thrust fault beneath the glacier, as was the case for the Libbey Glacier thrust in the upper part of the alpine valley.

The piedmont section of the glacier flows southwest toward Icy Bay with velocity generally decreasing toward the terminus and outward toward the ice margins (Figure 8). The western margin of the glacier is controlled by a steep cliff eroded into bedrock on the back-limb (western limb) of the Malaspina Fault propagation fold. A large band of medial moraine separates Agassiz and Malaspina Glaciers to the east (Figure 1). The moraine band is pockmarked by a chain of collapse pits that extend up-glacier from the terminus toward Oily Lake at the base of the Samovar Hills. There is little significant topographic relief at the base of the glacier where it abuts the moraine band (Figure 2) [*Conway et al.,* 2009]. Apparently, the piedmont lobe has not cut a deeply eroded trough, even though it flows along the crest and eastern forelimb of the Malaspina Fault propagation fold [*Chapman et al.*, 2012]. This implies that the rate of tectonic uplift during folding and faulting is sufficient to maintain the gentle undulating topography at the base of the glacier.

5. Discussion

5.1. Dimensional Scaling and Geologic Structure of Basal Ridges

Prior to discussing the tectonic significance of our results, we contemplate how glacial erosion modifies geologic structures at the base of the glacier. Rates of erosion by temperate glaciers are equal to, and often greater than, tectonic uplift by folding and faulting, which is typically several mm/yr in the Saint Elias orogeny [*Bruhn et al.*, 2010]. Where erosion at the base of the glacier equals that of uplift, relatively little if any relief will be generated. This may be the situation where Agassiz Glacier flows along the eastern limb of the Malaspina Fault propagation fold, for example.

The ridges beneath Malaspina Glacier perturb surface flow over areas ranging from ~10 km^2 to 40 km^2 (Figures 5–7, features W1 and E2), suggesting that the underlying ridges are at least several kilometers in size. The area of perturbed flow is a multivariate function of the size, shape, and topographic relief of the ridge, the depth of the ridge crest beneath the ice surface, and the ice flow velocity. Suitable 2-D functions that predict perturbations of glacier surface topography and flow rate exist for ideal sinusoidal-shaped ridges [*Gudmundsson,* 2003*; Raymond and Gudmundsson,* 2005], but to our knowledge not for complex 3-D ridge geometries that develop during erosion of folded sedimentary rock. However, conceptual insight into this problem can be gained from our studies of analogous areas in the Saint Elias orogen where glaciers have recently retreated exposing small mountain blocks with rocks similar to those beneath Malaspina Glacier [*Bruhn et al.*, 2010]. Below, we cite observations from Bering and Steller Glaciers, which flow onto the piedmont of the Saint Elias range ~100 km west of Malaspina Glacier and are located within a similar structural syntaxis with disparate trends of faults and folds [*Bruhn et al.*, 2004, 2010; *Chapman et al.*, 2012; *Pavlis et al.*, 2012]. Supporting observations from several laboratory experiments are also shown in the supporting information of this report (Figure S1).

Bruhn et al. [2010] investigated ice deformation above bedrock ridges during surging of the Bering Glacier in 1993–1994 [*Roush et al.*, 2003], and the structural geology of several other ridges located near the terminus of Steller Glacier are known from our own field observations and also mapping by *Taliaferro* [1932]. These examples include ridges that were elongated parallel to ice flow as well as those that plunged beneath the glacier at high angle to flow. The pattern of ice surface deformation during surging on Bering Glacier, for example, was similar to the parabolic-shaped refolding of moraine above ridge E2 on Malaspina Glacier during the surge in 1986–1987 (Figure 6) and to the small wrinkles developed on the surface of the laboratory experiment shown in the small inset in Figure 6. Part of the underlying ridge crest was subsequently exposed when Bering Glacier retreated, providing the opportunity to map the geologic structure in the summer of 2005. The ridge contained steeply dipping sandstone beds in the limb of a large northeast trending fold located on the hanging wall of a major thrust fault. The crest of the ridge did not coincide with the top or hinge zone of an anticline as one might guess. Rather, glacial abrasion and plucking created an elongated ridge with its crest parallel to the strike of dipping sedimentary layers in just one limb of the large asymmetrical anticline.

Small mountain blocks located at the terminus of the Steller Glacier provide examples where most of the ridge is now exposed for study (Figure S3a). Glacial erosion sculpted the rocks into ridges that are elongated parallel to the structural trend of the folded and faulted rocks. The rocks are interbedded sandstone, shale, and coal, similar to those presumed to lie beneath Malaspina Glacier. Each ridge contains at least one, and in some cases multiple folds (Figure S3b). Typical length to width ratios of the ice-sculpted ridges are ~3:1 for lengths ranging between 6 km and 13 km, respectively. Topographic relief scales upward with length and varies from several tens to as much as 200 m. The crest lines are asymmetrical, rising gently upward in the downflow direction and plunging downward more steeply at the distal or downflow end where ice plucking was most effective. These examples, like that cited previously from Bering Glacier, emphasize that an ice-sculptured ridge that is narrow and elongated parallel to ice flow may be formed by erosion of just part of one fold, or from parts of several folds. This ambiguity must be considered when inferring the structure beneath Malaspina Glacier.

Conversely, monoclinal flexures with axis at high angle to ice flow develop on the surface of a glacier where hinge lines of folded rocks are aligned at high angle to ice flow [*Bruhn et al.,* 2010]. Narrow canyons that represent part of the basal drainage network may cut through the underlying ridge, disrupting the continuity of the crest. The flanks of the ridges are asymmetric, with the steepest sloping and shortest flank on the downflow side. The relief of the monocline that develops on the surface of the glacier above this type of ridge may undulate because of the presence of underlying canyons and along-strike variation in the plunge of the crest as the ends of the ridge are reached.

Given the empirical scaling relationships cited above for ridges that are elongated parallel to ice flow, we consider plausible dimensions of ridge E2 (Figures 6 and 7) beneath the eastern sector of Malaspina Glacier. The narrowest hinge zone of refolded moraine is ~ 2.5 km to 3 km in width. If this width is similar to that of the ridge at depth, then the buried ridge may be 7 km to 9 km long, with topographic relief on the order of 100 m or more. We do not know if the ridge is sculpted from a single northwest trending anticline, or from several folds. Ridges E1 and W1 are presumably of similar size to E2 given the shape and size of the E1 gravity anomaly [*Allen and Smith,* 1953] and the spatial distribution of perturbed strain rate axes in the case of W1, where the crest of the inferred ridge is orientated at a higher angle to ice flow.

5.2. Esker Creek Fault and Tectonic Block Model

The disparate fault domains beneath the glacier are revealed by geophysical and geodetic data observations and modeling of coseismic displacement of shorelines in 1899 [*Estabrook et al.*, 1992; *Savage and Lisowski*, 1986; *Plafker and Thatcher*, 2008; *Elliott,* 2011; *Doser*, 2012]. However, the deep trough where ice flows across the Esker Creek fault is a recently documented geomorphic feature of note (Figure 2) [*Conway et al.,* 2009]. The narrow tongue of ice that flows westward along the range front into Oily Lake is presumably guided along this fault-cored trough and may create the sinuous ~ 2 km deflection of ice tongue T1 at the head of the glacier. An alternative, albeit more speculative hypothesis is that the deflection of tongue T1 reflects offset of the underlying basal river valley by dextral shearing along the Esker Creek fault. This hypothesis is plausible given the northwest direction of relative plate motion which resolves into downdip thrusting and dextral shearing on the ~ 30° north dipping fault surface [*Plafker and Thatcher,* 2008]. A related observation is that the trough of the Esker Creek fault is similar in depth and width to other glaciated strike-slip fault troughs in the orogen [*Plafker*, 1987; *Bruhn et al.*, 2012].

The Pamplona deformation front marks the eastern limit of terrane collision and accretion offshore (Figure 1). The deformation front has previously been extended onshore by connecting the easternmost thrust fault of the Pamplona belt to the Malaspina Fault, which lies beneath the piedmont lobe of Agassiz Glacier [*Plafker,* 1987*; Bruhn et al.,* 2004*; Worthington et al.,* 2010*; Chapman et al.,* 2012]. However, our results indicate that the deformation extends several tens of kilometers east of the Malaspina Fault that is beneath the western sector of the glacier shown in Figure 7. Two independent lines of evidence further support our contention. (1) Stratigraphic data from petroleum exploration wells located along the shores of Icy Bay show a marked change in stratigraphy that is best explained by the presence of a northeast striking thrust fault located beneath the boundary between Agassiz and Malaspina Glaciers, several kilometers east of the Malaspina Fault [*Chapman et al.,* 2012]. (2) Recently acquired geodetic data require ~ 1 cm/yr crustal shortening beneath Malaspina Glacier [*Elliott*, 2011]. This led *Elliott* [2011] to model a small tectonic block beneath the Malaspina Glacier that was bounded on the east by a thrust fault that accommodated the requisite shortening. All of

these results indicate that the easternmost thrust of the Pamplona deformation front must in some manner link to one or more northeast structures beneath the western sector of Malaspina Glacier. These structures terminate where they intersect the northwest trending structures beneath the eastern sector of the glacier (Figure 7). This complex zone of structural intersection may be responsible for the intense crustal seismicity and complex strain field indicated by focal mechanisms [*Horner*, 1983; *Estabrook et al*., 1992; *Doser*, 2012].

5.3. Geological Control of Seismicity and Earthquake Rupture

The earthquake geology of the terrain beneath Malaspina Glacier is speculative because geological evidence is buried by ice and the seismological data for the large earthquakes in 1899 are sparse and of limited quality [*Plafker and Thatcher*, 2008]. However, the structural syntaxis must be a zone of highly fractured and faulted rocks where secondary deformation offsets and warps major thrust fault surfaces. The complex structure mapped in the Samovar Hills suggests that the underlying intersection between the Malaspina and Esker Creek faults is a zone of distributed faulting and fracturing [*Chapman et al.*, 2012]. The depression occupied by Oily Lake is located at the structural groin formed by the intersection line and presumably reflects glacial scouring of the intensely fractured rock created around the fault intersection. This zone of distributed deformation presumably continues beneath the glacier along the trace of the syntaxis.

A broad zone of concentrated secondary deformation where faults of different orientation intersect forms a barrier to rupture propagation that will certainly inhibit, and often arrest, rupturing as slip is transferred from one primary fault surface to an adjoining one [*King*, 1983]. The result may be delayed triggering of slip between two major earthquakes, as stress from the arrested rupture is transferred either by elastic or viscoelastic deformation onto the adjacent fault(s). This may have been the case in 1899, when two *Mw* 8.1 earthquakes rocked the regions surrounding Malaspina Glacier within 6 days [*Tarr and Martin*, 1912]. The Yakutat Bay earthquake on 10 September was preceded by an *Mw* 8.1 earthquake on 4 September that ruptured thrust faults within the area between Malaspina Glacier and Cape Yakataga to the west. Presumably, this was a case of delayed earthquake triggering, where the 4 September rupture of east to northeast striking thrust faults arrested beneath Malaspina Glacier, transferring stress onto the northwest striking coastal thrust system that then failed on 10 September. Although the exact faults and focal mechanisms for the 4 September are uncertain [*Plafker and Thatcher*, 2008], we ran Coulomb stress transfer calculations using the program Coulomb 3.2 [*Toda et al.*, 2005; *Lin and Stein*, 2004]. For most faulting scenarios we considered, faulting on the Esker Creek fault would be promoted by the stress transfer in the event on 4 September.

6. Conclusions

1. Using suites of Landsat TM images collected over periods of several days to years and a pair of ALOS PALSAR scenes, we successfully estimated ice velocities using feature tracking on the Malaspina Glacier through image cross correlation. The pattern of surface flow on the glaciers was in turn used to infer locations and orientations of topographic features at the base of the glacier. Recognition that the glacier overlies two disparate structural domains provides a geological framework for interpreting the nature of seismicity and crustal strain surrounding Malaspina Glacier.
2. Malaspina Glacier is underlain by a structural syntaxis formed where the northwest trending structures of the Fairweather part of the plate boundary intersect northeast trending structures that accommodate collision and accretion of the Yakutat Terrane. The axis of the syntaxis divides two disparate structural domains, one associated with the Fairweather fault part of the plate boundary and the second related to the onset of collision and accretion of the Yakutat Terrane.
3. The mapped structural domains beneath Malaspina Glacier require that deformation associated with collision and accretion of the Yakutat Terrane begins several tens of kilometers farther east than previously suggested. The deformation front beneath the glacier occurs along the axial trace of the structural syntaxis rather than at the Malaspina Fault.
4. The subglacier syntaxis is a locus of intense crustal seismicity that partially accommodates the complex strain field surrounding the axial trace of the structural syntaxis. The axis of the syntaxis may also be an important earthquake rupture barrier based on the aerial extent and temporal delay in rupturing of two *Mw* 8.1 earthquakes in September 1899.

Acknowledgments

National Aeronautics and Space Administration (NASA) grant entitled "Geodetic Imaging of Glacio-seismotectonic Processes in Southern Alaska" (NNX08AX88G) awarded to J. Sauber, R. R. Forster, and R. L. Bruhn supported this research. J. Sauber was also supported by funding from the NASA 2012 Science Innovation Fund at Goddard Space Flight Center. E. Burgess was funded under the NASA Earth Science Space Fellowship. E. Burgess and R.R. Forster were also partially supported by NASA grant NNX08AP27G. We thank the editors at Tectonics and those who reviewed the manuscript, J. B. Chapman and L. Stearns, for their input and help.

References

Allen, C. R., and G. I. Smith (1953), Seismic and gravity investigations on the Malaspina Glacier, Alaska, *Trans. Am. Geophys. Union*, *34*(5), 755–760, doi:10.1029/TR034i005p00755.

Allen, C. R., and R. P. Sharp (1953), Deformation of bore hole in Malaspina glacier, Alaska, *GSA Bull.*, *64*(1), 97–100, doi:10.1130/0016-7606(1958)69[617:MGA]2.0.CO;2.

Bruhn, R. L., T. L. Pavlis, G. Plafker, and L. Serpa (2004), Deformation during terrane accretion in the Saint Elias orogen, Alaska, *Geol. Soc. Am. Bull.*, *116*, 771–787, doi:10.1130/B25182.1.

Bruhn, R. L., R. R. Forster, A. L. J. Ford, T. L. Pavlis, and M. Vorkink (2010), Structural geology and glacier dynamics, Bering and Stellar Glaciers, Alaska, *Geol. Soc. Am. Special Pap.*, *462*, 217–233, doi:10.1130/2010.2462(11).

Bruhn, R. L., J. Sauber, M. M. Cotton, T. L. Pavlis, E. Burgess, N. Ruppert, and R. R. Forster (2012), Plate margin deformation and active tectonics along the northern edge of the Yakutat Terrane in the Saint Elias Orogen, Alaska, and Yukon, Canada, *Geosphere*, *8*(6), 1384–1407, doi:10.1130/GES00807.1.

Burgess, E. W., R. R. Forster, and C. F. Larsen (2013), Flow velocities of Alaska glaciers, *Nat. Commun.*, *4*, 1–8, doi:10.1038/ncomms3146.

Cardozo, N., and R. W. Allmendinger (2009), SSPX: A program to compute strain from displacement/velocity data, *Comput. Geosci.*, *35*, 1343–1357, doi:10.1016/j.cageo.2008.05.008.

Chapman, J. B., T. L. Pavlis, R. L. Bruhn, L. L. Worthington, S. Gulick, and A. Berger (2012), Structural relationships in the eastern syntaxis of the St. Elias orogen, Alaska, *Geosphere*, *8*(1), 105–126, doi:10.1130/GES00677.1.

Conway, H., B. Smith, P. Vaswani, K. Matsuoka, E. Rignot, and P. Claus (2009), A low-frequency ice-penetrating radar system adapted for use from an airplane: Test results from Bering and Malaspina Glaciers, Alaska, U.S.A., *Ann. Glaciol.*, *50*, 93–97, doi:10.3189/172756409789097487.

Cuffey, K., and W. Paterson (2010), *The Physics of Glaciers*, 4th ed., Academic Press, Burlington, Mass.

Doser, D. I. (2012), Revisiting the 1979 St. Elias, Alaska, aftershock sequence and its regional significance, *Bull. Seismol. Soc. Am.*, *2*, 2392–2404, doi:10.1785/0120120007.

Elliott, J. (2011), Active tectonics in southern Alaska and the role of the Yakutat block constrained by GPS measurements, PhD dissertation, Dep. of Geol. and Geophys., Univ of Alaska, Fairbanks, Alaska, U.S.A.

Enkelmann, E., P. K. Zeitler, T. L. Pavlis, J. I. Garver, and K. D. Ridgway (2009), Intense localized rock uplift and erosion in the St Elias orogen of Alaska, *Nat. Geosci.*, *2*, 360–363, doi:10.1038/ngeo502.

Estabrook, C. H., J. L. Nabelek, and J. L. Lerner-Lam (1992), Tectonic model of the Pacific-North American plate boundary in the Gulf of Alaska from broadband analysis for the 1979 St. Elias, Alaska, earthquake and its aftershocks, *J. Geophys. Res.*, *97*, 6587–6612, doi:10.1029/92JB00131.

Farr, T., and M. Kobrick (2000), Shuttle Radar Topography Mission produces a wealth of data, *Eos Trans. AGU*, *81*, 583–585, doi:10.1029/EO081i048p00583.

Ford, A. L., R. R. Forster, and R. L. Bruhn (2003), Ice surface velocity patterns on Seward Glacier, Alaska/Yukon, and their implication for regional tectonics in the Saint Elias Mountains, *Ann. Glaciol.*, *36*, 21–28, doi:10.3189/172756403781816086.

Gudmundsson, G. (2003), Transmission of basal variability to a glacier surface, *J. Geophys. Res.*, *108*(B5), 2253, doi:10.1029/2002JB002107.

Gustavson, T. C., and J. C. Boothroyd (1987), A depositional model for outwash, sediment sources, and hydrologic characteristics, Malaspina Glacier, Alaska: A modern analog of the southeastern margin of the Laurentide Ice Sheet, *Geol. Soc. Am. Bull.*, *99*, 187–200, doi:10.1130/0016-7606.

Horner, R. B. (1983), Seismicity in the St. Elias region of northwestern Canada and southeastern Alaska, *Bull. Seismol. Soc. Am.*, *73*(4), 1117–1137.

King, G. (1983), The accommodation of large strains in the upper lithosphere of the Earth and other solids by self-similar fault systems: The geometrical origin of B-value, *Pure Appl. Geophys.*, *121*, 761–815, doi:10.1007/BF02590182.

Koons, P. O., B. P. Hooks, T. Pavlis, P. Upton, and A. D. Barker (2010), Three-dimensional mechanics of Yakutat convergence in the southern Alaskan plate corner, *Tectonics*, *29*, TC4008, doi:10.1029/2009TC002463.

Krabill, W. B., W. Abdalati, E. B. Frederick, S. S. Manizade, C. F. Martin, J. G. Sonntag, R. N. Swift, R. H. Thomas, and J. G. Yungel (2002), Aircraft laser altimetry measurements of changes of the Greenland ice sheet: Technique and accuracy assessment, *J. Geodyn.*, *34*(3–4), 357–376, doi:10.1016/S0264-3707(02)00040-6.

Leprince, S., F. Ayoub, Y. Klingert, and J. P. Avouac (2007a), Co-Registration of Optically Sensed Images and Correlation (COSI-Corr): An operational methodology for ground deformation measurements, *Geosci. Remote Sens. Symp.*, 1943–1946, doi:10.1109/IGARSS.2007.4423207.

Leprince, S., S. Barbot, F. Ayoub, and J. P. Avouac (2007b), Automatic and precise orthorectification, coregistration, and subpixel correlation of satellite images, application to ground deformation measurements, *Geosci. Remote Sens., IEEE Trans.*, *45*, 1529–1558, doi:10.1109/TGRS.2006.888937.

Lin, J., and R. S. Stein (2004), Stress triggering in thrust and subduction earthquakes, and stress interaction between the southern San Andreas and nearby thrust and strike-slip faults, *J. Geophys. Res.*, *109*, B02303, doi:10.1029/2003JB002607.

Molnia, B. F., and J. E. Jones (1989), View through ice: Are unusual airborne radar backscatter features from the surface of the Malaspina glacier, Alaska. Expressions of subglacial morphology?, *Eos Trans. AGU*, *70*, 701–701, doi:10.1029/89EO0022.

Muskett, R. R., C. S. Lingle, W. V. Tangborn, and B. Rabus (2003), Multi-decadal elevation changes on Bagley Ice Valley and Malaspina Glacier: Alaska, *Geophys. Res. Lett.*, *30*(16), 1857, doi:10.1029/2003GL017707.

Muskett, R. R., C. S. Lingle, J. M. Sauber, A. S. Post, W. V. Tangborn, and B. T. Rabus (2008), Surging, accelerating surface lowering and volume reduction of the Malaspina Glacier system, Alaska, U.S.A., and Yukon, Canada, from 1972 to 2006, *J. Glaciol.*, *54*(188), 788–800, doi:10.3189/002214308787779915.

Pavlis, T. L., J. B. Chapman, R. L. Bruhn, K. Ridgeway, L. L. Worthington, S. P. S. Gulick, and J. Spotila (2012), Structure of the actively deforming fold-thrust belt of the St. Elias orogeny with implication for glacial exhumation and three-dimensional tectonic processes, *Geosphere*, *8*, 991–1019, doi:10.1130/GES00753.1.

Plafker, G. (1987), Regional geology and petroleumpotential of the northern Gulf of Alaska continentalmargin, *Earth Sci. Series*, pp. 229–226, Geology and Resource Potential of the Western North American and Adjacent Ocean Basins – Beaufort Sea to Baja California, Houston, Tex.

Plafker, G., and W. Thatcher (2008), Geological and geophysical evaluation of the mechanisms of the great 1899 Yakutat Bay earthquakes, in *Active Tectonics and Seismic Potential of Alaska*, *Geophys. Monogr. Ser.*, 179, pp. 215–236, AGU, Washington, D. C., doi:10.1029/179GM12.

Raymond, M. J., and G. H. Gudmundsson (2005), On the relationship between surface and basal properties on glaciers, ice sheets, and ice streams, *J. Geophys. Res.*, *110*, B08411, doi:10.1029/2005JB00368.

Rignot, E., J. Mouginot, C. F. Larsen, Y. Gim, and D. Kirchner (2013), Low-frequency radar sounding of temperate ice masses in Southern Alaska, *Geophys. Res. Lett.*, *40*, 5399–5405, doi:10.1002/2013GL057452.

Rosenqvist, A., M. Shimada, N. Ito, and M. Watanabe (2007), ALOS PALSAR: A pathfinder mission for global-scale monitoring of the environment, *IEEE Trans. Geoscience Remote Sens.*, *45*(11), 3307–3316, doi:10.1109/TGRS.2007.901027.

Roush, J. J., C. S. Lingle, R. M. Guritz, D. R. Fatland, and V. A. Voronina (2003), Surge-front propagation and velocities during the early-1993–95 surge of Bering Glacier, Alaska, U.S.A., from sequential SAR imagery, *Ann. Glaciol.*, *36*, 37–44, doi:10.3189/172756403781816266.

Sauber, J., B. Molnia, C. Carabajal, S. Luthcke, and R. Muskett (2005), Ice elevations and surface change on the Malaspina Glacier, Alaska, *Geophys. Res. Lett.*, *32*, L23S01, doi:10.1029/2005GL023943.

Savage, J. C., and M. Lisowski (1986), Strain accumulation in the Yakataga Seismic Gap, southern Alaska, *J. Geophys. Res.*, *91*(B9), 9495–9506, doi:10.1029/JB091iB09p09495.

Sharp, R. P. (1958), Malaspina Glacier, Alaska, *Geol. Soc. Am. Bull.*, *69*, 617–646, doi:10.1130/0016-7606(1958)69[617:MGA]2.0.CO;2.

Strozzi, T., A. Luckman, T. Murray, U. Wegmuller, and C. L. Werner (2002), Glacier motion estimation using SAR off set-tracking procedures, *IEEE Trans. Geosci. Remote Sens.*, *40*(11), 2384–2391, doi:10.1109/TGRS.2002.805079.

Taliaferro, N. L. (1932), Geology of the Yakataga, Katalla, and Nichwak districts, Alaska, *Geol. Soc. Am. Bull.*, *43*, 749–782.

Tarr, R. S., and L. Martin (1912), *The Earthquakes of Yakutat Bay, Alaska in September 1899*, *U.S. Geol. Surv. Prof. Pap.*, vol. 69, 135 pp., U.S. Gov't. Print. Off., Washington.

Toda, S., R. S. Stein, K. Richards-Dinger, and S. Bozkurt (2005), Forecasting the evolution of seismicity in southern California: Animations built on earthquake stress transfer, *J. Geophys. Res.*, B05S16, doi:10.1029/2004B003415.

Turrin, J., R. R. Forster, C. Larsen, and J. Sauber (2013), The propagation of a surge front on Bering Glacier, Alaska, 2001–2011, *Ann. Glaciol.*, *54*(63), 221–228, doi:10.3189/2013AoG63A341.

Worthington, L. L., S. P. S. Gulick, and T. L. Pavlis (2010), Couple stratigraphic and structural evolution of a glaciated orogenic wedge, offshore St. Elias orogen, Alaska, *Tectonics*, *29*, TC6013, doi:10.1029/2010TC002723.

Worthington, L. L., H. J. A. Van Avendonk, S. P. S. Gulick, G. L. Christeson, and T. L. Pavlis (2012), Crustal structure of the Yakutat terrane and the evolution of subduction and collision in southern Alaska, *J. Geophys. Res.*, *117*, B01102, doi:10.1029/2011JB008493.